Nano Research 2015, 8(5): 1637–1647
DOI 10.1007/s12274-014-0653-2
Research Article

ISSN 1998-0124
CN 11-5974/O4

Real-time *in vivo* visualization of tumor therapy by a near-infrared-II Ag_2S quantum dot-based theranostic nanoplatform

Feng Hu[§], Chunyan Li[§], Yejun Zhang, Mao Wang, Dongming Wu, and Qiangbin Wang (✉)

Key Laboratory of Nano-Bio Interface, Division of Nanobiomedicine and i-Lab, Suzhou Institute of Nano-Tech and Nano-Bionics, Chinese Academy of Sciences, Suzhou 215123, China
[§] *These authors contributed equally to this work.*

Received: 13 Octobrt 2014
Revised: 18 November 2014
Accepted: 21 November 2014

KEYWORDS

in vivo imaging,
Ag_2S quantum dots,
second near-infrared window fluorescence,
drug delivery,
tumor therapy

ABSTRACT

Real-time and objective feedback of therapeutic efficacies would be of great value for tumor treatment. Here, we report a smart Ag_2S QD-based theranostic nanoplatform (DOX@PEG–Ag_2S) obtained by loading the anti-cancer drug doxorubicin (DOX) into polyethylene glycol-coated silver sulfide quantum dots (PEG–Ag_2S QDs) through hydrophobic–hydrophobic interactions, which exhibited high drug loading capability (93 wt.% of DOX to Ag_2S QDs), long circulation in blood ($t_{1/2}$ = 10.3 h), and high passive tumor-targeting efficiency (8.9% ID/gram) in living mice where % ID/gram reflects the probe concentration in terms of the percentage of the injected dose (ID) per gram of tissue. After targeting the tumor tissue, DOX from PEG–Ag_2S cargoes was selectively and rapidly released into cancer cells, giving rise to a significant tumor inhibition. Owing to the deep tissue penetration and high spatio-temporal resolution of Ag_2S QDs fluorescence in the second near-infrared window (NIR-II), the DOX@PEG–Ag_2S enabled real-time *in vivo* reading of the drug targeting process and therapeutic efficacy. We expect that such a novel theranostic nanoplatform, DOX@PEG–Ag_2S, with integrated drug delivery, therapy and assessment functionalities, will be highly useful for personalized treatments of tumors.

1 Introduction

Cancer imposes a great threat on people's lives due to its covert characteristics, extensive drug resistance and propensity to relapse [1]. Since real-time visualization of these therapeutic courses is very important for clinicians to rapidly assess whether a drug is effective in an individual patient or not, extensive efforts have been devoted to designing multifunctional nanoplatforms for theranostics of tumors, including liposomes [2, 3], polymers [4, 5], mesoporous silica nanoparticles [6–8], magnetic nanocrystals [9–11] and

Address correspondence to qbwang2008@sinano.ac.cn

gold nanoparticles [12–18]. However, it remains great challenging to meet the theranostic goal due to the enhanced reticuloendothelial system (RES) uptake, nonspecific drug release and low spatial resolution of *in vivo* imaging [19]. In particular, few systems can provide real-time feedback during the course of tumor treatment for the assessment and improvement of therapeutic efficacies.

Quantum dots (QDs) emitting in the second near-infrared window (NIR-II, 1,000–1,400 nm) might be an ideal platform to provide real-time visualization of the *in vivo* theranostic process by rationally integrating various functionalities [20–24]. Our previous results have successfully illustrated that Ag_2S QDs, as a new type of NIR-II QDs, possess appealing features for *in vivo* imaging including (1) large tissue penetration depth (1.2 cm), (2) high spatial resolution (25 μm) and temporal resolution (50 ms), (3) long circulation time ($t_{1/2}$ = 4.37 h) after coating with polyethylene glycol (PEG) and (4) high tumor uptake (10% ID/gram tumor accumulation after 72 h post injection, where % ID/gram reflects the probe concentration in terms of the percentage of the injected dose (ID) per gram of tissue) [25–30]. Such advantageous properties make Ag_2S QDs an ideal probe to detect early-stage tumors and image the *in vivo* dynamic process of tumor treatment. Here, we reported that PEG–Ag_2S QDs act as a novel theranostic nanoplatform that enables *in vivo* simultaneous diagnosis, drug delivery and therapeutic monitoring of tumors by loading with a typical anti-cancer drug, doxorubicin (DOX), as a demonstration.

2 Experimental

2.1 Materials

All chemicals were analytical grade and used without further purification. 1-Dodecanethiol (DT), chloroform, dichloromethane and triethylamine were purchased from Aladdin or Sinopharm Chemical Reagent Co., Ltd. (China). *N*-(3-dimethylaminopropyl)-*N*-ethylcarbodiimide hydrochloride (EDC) was obtained from Sigma Aldrich. 5k PEG polymer was purchased from Beijing Kaizheng Bio Inc. Doxorubicin hydrochloride (DOX–HCl) was purchased from Sangon Biotech. Deionized water was used in all experiments.

2.2 Synthesis of DT-coated Ag_2S QDs (DT-Ag_2S)

DT–Ag_2S in an organic phase and the single source precursor of $(C_2H_5)_2NCS_2Ag$ (Ag(DDTC)) were synthesized according to our previous reports [25, 30]. In a typical synthetic process, 0.1 mmol of Ag(DDTC) was added to 10 g of DT in a three-necked flask (100 mL) at room temperature. Then, oxygen was removed from the slurry with vigorous magnetic stirring under vacuum for 5 min. The reaction temperature was then raised to 150 ℃ at a rate of 10 ℃/min and the mixture kept at this temperature for 2 min to allow the growth of Ag_2S QDs under N_2 atmosphere. After the reaction, 2.8 nm-sized DT-Ag_2S were obtained, which were freely soluble in chloroform.

2.3 Synthesis of C18PMH/PEG

Poly(maleic anhydride-alt-1-octadecene)– polyethylene glycol (C18PMH/PEG) was synthesized according to a previously reported method with a minor modification [31]. Briefly, 30 mg of C18PMH was reacted with 429 mg of 5k PEG in 15 mL of dichloromethane for 24 h in the presence of 33 mg of EDC and 18 μL of triethylamine. After 24 h of stirring, the dichloromethane was blown dry by N_2. The residual solid was then dissolved in water, forming a transparent solution, which was dialyzed against distilled water for 48 h in a dialysis bag with a molecular weight cutoff (MWCO) of 8–14 kDa to remove unreacted PEG. After lyophilization, the product in a white solid was finally stored at –20 ℃ for future use.

2.4 Synthesis of water-soluble C18PMH/PEG–Ag_2S QDs (PEG–Ag_2S)

A portion of 100 mg C18PMH/PEG was added into 10 mL of $CHCl_3$ containing as-synthesized DT–Ag_2S, and then the solution was stirred for 2 h at room temperature after a minor sonication. The chloroform was blown dry by N_2, and then the remnant was dissolved in phosphate buffered saline (PBS, pH = 7.4). All the DT–Ag_2S was transferred into the water after capping the C18PMH/PEG via hydrophobic interaction.

2.5 Characterization

Transmission electron microscope (TEM) images were obtained with a Tecnai G2 F20 STwin TEM (FEI, U.S.A.)

operated at 200 kV. The UV–vis–NIR absorption spectra were recorded on a Lambda-750 spectrometer (Perkin-Elmer) at room temperature. The NIR-II fluorescence spectra were collected on an Applied NanoFluorescence spectrometer at room temperature with an excitation laser source of 785 nm. Fourier transform infrared spectroscopy (FTIR) spectra were recorded on a Nicolet 6700 spectrometer. Inductively coupled plasma atomic emission spectroscopy (ICP–AES) (Optima 7300DV, Perkin-Elmer) was used to measure the concentrations of Ag_2S QDs. Dynamic laser scattering measurement of Ag_2S QDs was performed on a Zetasizer Nano ZS (Malvern).

2.6 Drug loading and *in vitro* release

DOX–HCl (5 mg) was added to 500 μL DMSO and solubilized by the addition of 3 μL of triethylamine with sonication. The hydrophobic DOX in DMSO then mixed with 10 mL of PEG–Ag_2S in PBS (pH = 7.4) followed by stirring for 24 hours. Free DOX was removed through ultrafiltration using an Amicon Ultra-15 Centrifugal Filter Unit with 100 kDa MW cut-off (Millipore). The loading efficiency of DOX in the PEG–Ag_2S was calculated by following formula: Loading efficiency (wt.%) = (initial amount DOX-residual DOX)/weight of Ag_2S.

The DOX release in PBS with pH 7.4 and 5.5 was performed by transforming 1 mL of DOX@PEG–Ag_2S to a dialysis bag with a molecular weight cutoff of 8–14 kDa immersed in 50 mL of PBS with pH 7.4 or 5.5 at a constant temperature with gentle stirring. At selected time intervals, 200 μL of buffered solution outside the dialysis bag was collected for analysis and then replaced with an equal volume of fresh PBS buffer. The amounts of released DOX were measured by UV–vis–NIR absorbance spectroscopy.

2.7 Cell culture and cytotoxicity assay

MDA-MB-231 human breast cancer cells were purchased from the Cell Bank of Type Culture Collection of the Chinese Academy of Sciences. Cells were grown in RPMI 1640 medium (Hyclone) supplemented with 10% FBS (fetal bovine serum) at 37 °C under 5% CO_2. *In vitro* cytotoxicity studies of various Ag_2S QDs on MDA-MB-231 cells were performed by using a standard MTT (3-(4,5-dimethylthiazol-2-yl)-2,5-diphenyltetrazolium bromide) assay. Briefly, cells were cultured overnight in 96-well plates (5×10^3 cells per well) to allow cell attachment, and then incubated with 200 μL of fresh cell media containing various Ag_2S QDs (DOX at concentrations of 0, 9, 18, 37.5, 75, and 150 μM) for 72 h. The combined MTT/PBS solution was added to each well of the 96-well assay plate, and incubated for an additional 4 h. An enzyme-linked immunosorbent assay (ELISA) reader (infinite M200, Tecan, Austria) was used to measure the OD570 (Absorbance value) of each well referenced at 690 nm. The following formula was used to calculate the viability of cell growth:

Viability (%) = (mean of Absorbance value of treatment group/mean Absorbance value of control) × 100.

2.8 *In vivo* anti-cancer assay

All animals were obtained from Shanghai SLRC Laboratory Animal Co. and the experiments were performed with the Guidelines for the Care and Use of Research Animals. MDA-MB-231 human breast tumor cells (1×10^6) were subcutaneously injected into the right leg of the 6-week-old female nude mice. The tumor was allowed to reach ~2 mm in diameter and the mice then randomly divided into four different groups ($n = 6$ for each group). PBS, DOX, PEG–Ag_2S or DOX@PEG–Ag_2S (DOX at a concentration of 1.5 mg/mL, Ag_2S at a concentration of 1.6 mg/mL, 200 μL) was intravenously injected into the mice for five times at different timepoints (day 1, 4, 7, 10 and 13). To monitor the tumor weight, the mice was sacrificed by cervical dissociation one week after the treatment was finished, and the tumors were removed from the mice and weighed. Tumor volume was estimated according to the formula $V = 0.52ab^2$, where a is the largest superficial diameter and b is the smallest superficial diameter.

2.9 *In vivo* imaging

A portion of 200 μL DOX@PEG–Ag_2S at a 1.5 mg/mL (DOX) concentration was injected intravenously into nude mice. During injection and imaging, the mice were anesthetized using a 2 L/min oxygen flow with 2% isoflurane. NIR-II fluorescence images were collected using a two-dimensional InGaAs array (Photonic Science) for collecting photons in NIR-II. The excitation

light was provided by an 808 nm diode laser and filtered by an 880 nm long-pass filter. The excitation power density at the imaging plane was 45 mW/cm^2. The emitted light from the animal was filtered through a 1,100 nm long-pass filter coupled with the InGaAs camera for NIR-II imaging.

2.10 Histology

To test the *in vivo* toxicity, DOX@PEG–Ag_2S (DOX at a concentration of 1.5 mg/mL, 200 μL) was intravenously injected into healthy mice and then the mice were sacrificed at day 3. Major organs including heart, liver and kidney were harvested, fixed in 4% formalin/PBS solution, and embedded in optical cutting temperature (OCT) resin. Tissue samples were further stained with hematoxylin and eosin and subsequently imaged via light microscopy (Nikon Eclipse 80i microscope, Japan).

2.11 Data analysis

Data are expressed as mean ± standard deviation. The statistical difference between two groups was determined using an unpaired, two-tailed t test. *p*-values less than 0.05 were considered statistically significant.

3 Results and discussion

Figure 1(a) depicts the design and preparation of DOX@PEG–Ag_2S theranostic nanoplatform. First, 1-dodecanethiol-coated Ag_2S QDs (DT–Ag_2S) were hydrophilized using PEG-grafted amphiphilic poly(maleic anhydride-alt-1-octadecene)-methoxy poly(ethylene glycol) [C18PMH/PEG] (denoted as PEG–Ag_2S) via hydrophobic–hydrophobic interaction between DT and the octadecene of C18PMH/PEG. Secondly, the hydrophobic DOX drug was encapsulated in the hydrophobic zone of PEG–Ag_2S with a high DOX loading capacity (93 wt.% relative to Ag_2S QDs). The DOX-loaded PEG–Ag_2S (denoted as DOX@PEG–Ag_2S) presented an increased drug dissociation rate in an acidic environment, favorable for controlled drug release. As illustrated in Fig. 1(b), when injected into mice by the tail vein, DOX@PEG–Ag_2S can gradually inflow into the tumor allowing retention of loaded drugs for a long period of time and, eventually, achieve a high accumulation of the drug at the target site via the enhanced permeability and retention (EPR) effect and lead to efficient tumor suppression. Meanwhile, the NIR-II emission of Ag_2S QDs featuring large tissue penetration depth and high spatio-temporal resolution facilitate the real-time *in vivo* visualization of the drug delivery process and the therapeutic efficacy with high fidelity.

Figure 2(a) shows a typical transmission electron microscopy (TEM) image of the as-synthesized PEG–Ag_2S from DT–Ag_2S (Fig. S1 in the Electronic Supplementary Material (ESM)), in which the PEG–Ag_2S was well dispersed, indicating complete protection

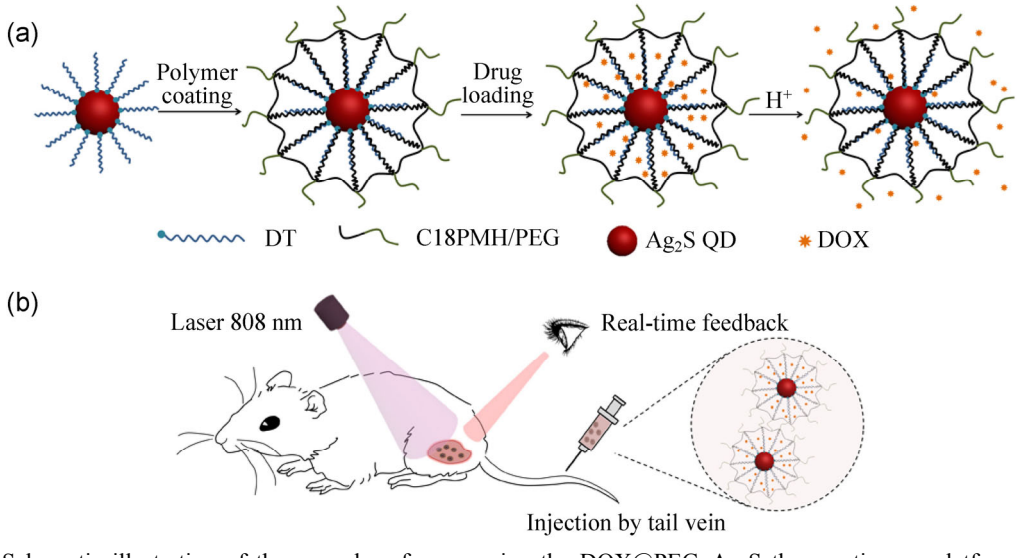

Figure 1 (a) Schematic illustration of the procedure for preparing the DOX@PEG–Ag_2S theranostic nanoplatform. (b) Schematic diagram of real-time visualization of tumor therapy using the DOX@PEG–Ag_2S theranostic nanoplatform.

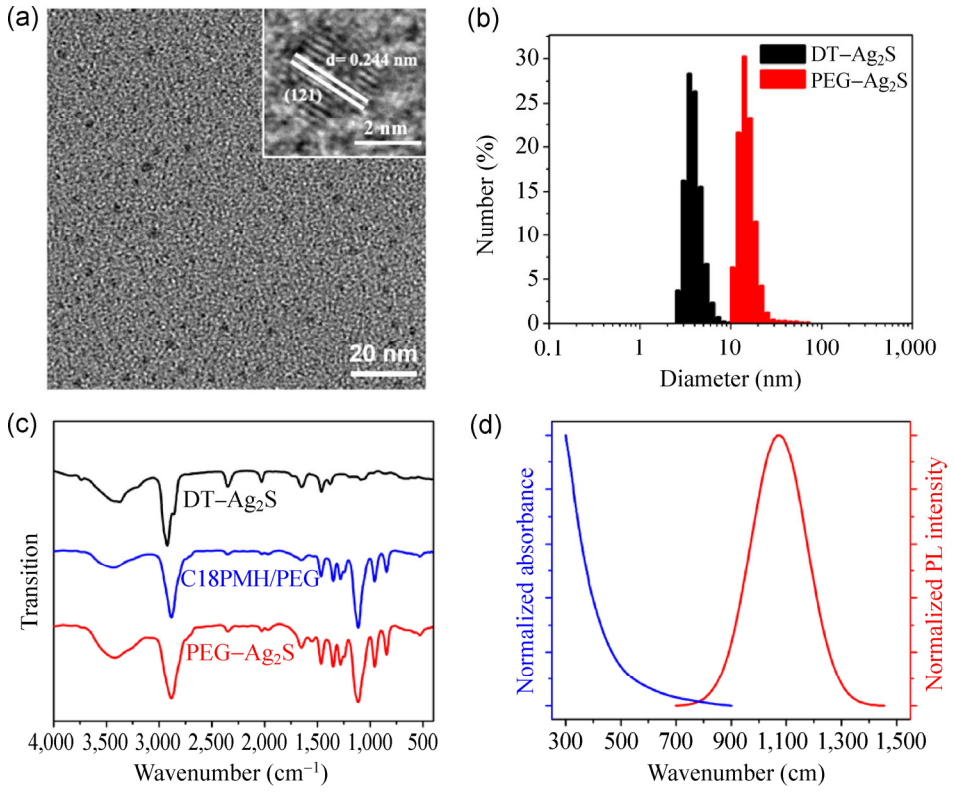

Figure 2 Characterization of PEG–Ag_2S. (a) TEM and HR-TEM (inset) images of PEG–Ag_2S. (b) The hydrodynamic diameters of DT–Ag_2S (3.6 nm) and PEG–Ag_2S (13.4 nm). (c) FTIR spectra of the DT–Ag_2S, C18PMH/PEG, and PEG–Ag_2S. (d) Normalized UV–vis–NIR absorbance and fluorescence emission spectra of PEG–Ag_2S.

and passivation of the QD surface by the PEG chains. The successful coating of C18PMH/PEG on the Ag_2S QDs surface was also evidenced by dynamic laser scattering (DLS) measurements (Fig. 2(b)) and Fourier transform infrared (FTIR) spectroscopy (Fig. 2(c)). The hydrodynamic diameter of PEG–Ag_2S obtained by DLS is about 13.4 nm, which is larger than that of the DT–Ag_2S (3.6 nm) dispersed in chloroform, verifying the presence of the polymer coating on the surface of Ag_2S QDs. The appearance of a new peak located at 1,110 cm^{-1} in the FTIR spectrum of PEG–Ag_2S corresponding to the stretching vibration of the ether bond of PEG chains further confirms the successful coating of C18PMH/PEG on the Ag_2S QDs surface. Figure 2(d) shows the absorption and emission spectra of the PEG–Ag_2S, which are similar to those of DT–Ag_2S (Fig. S2(a), in the ESM) without any obvious change after coating with the polymer. Further, the quantum yield and lifetime of the as-prepared PEG–Ag_2S was measured to be 17% and 61 ns, respectively.

The coating of C18PMH/PEG on the DT–Ag_2S QDs surface not only affords hydrophilicity of Ag_2S QDs but also serves as an ideal drug-loading layer for encapsulating lipophilic drugs [32]. On adding hydrophobic DOX to the PEG–Ag_2S with stirring under light-protected conditions, DOX-loaded PEG–Ag_2S (DOX@PEG–Ag_2S) was obtained as an effective drug delivery system. As shown in Fig. S2(b) (in the ESM), a characteristic peak of DOX at ~490 nm in the UV–vis–NIR absorption spectrum indicates the successful encapsulation of DOX in PEG–Ag_2S. The encapsulated amount of DOX was determined to be 93 wt.% (as a weight percentage of DOX relative to Ag_2S QDs) by UV–vis–NIR absorption spectroscopy and inductively coupled plasma–mass spectrometry (ICP–MS). It is worth noting that the NIR-II fluorescence of Ag_2S QDs shows a minimal change after the loading of DOX which allows real-time reading of the dynamic processes of drug delivery and tumor therapy. Meanwhile, DOX fluorescence was largely quenched

in the DOX@PEG–Ag_2S sample due to the absorbance of Ag_2S QDs; however, the fluorescence was recovered after dissociation from PEG–Ag_2S enabling the monitoring of DOX release (Fig. S3, in the ESM) [32, 33].

On-demand release is critical for a successful drug delivery system. We carefully examined the DOX release dynamics from DOX@PEG–Ag_2S under different pH conditions of 5.5 and 7.4 which mimic the tumor microenvironment and normal physiological conditions, respectively. As shown in Fig. 3(a), under normal physiological conditions (PBS, pH = 7.4), DOX@PEG–Ag_2S showed relatively low release rate. After incubation at 37 ℃ for 24 h, less than half of DOX was released from PEG–Ag_2S. In contrast, under extracellular conditions mimicking cancer cells (PBS, pH = 5.5), the release of DOX from DOX@PEG–Ag_2S became fast and maintained a steady release rate with increasing incubation time and 90% of DOX was released after incubation for 24 h. We attribute the accelerated release dynamics to the protonation of DOX molecules under acidic conditions, which gives DOX a positive charge and weakens its van der Waals interactions with the hydrophobic chains on the Ag_2S surface [32, 34]. These results indicate that the DOX@PEG–Ag_2S can be an ideal tumor microenvironment-responsive drug delivery system for tumor treatment.

To test the therapeutic effect of the DOX@PEG–Ag_2S, *in vitro* cell viability was quantified by means of MTT assay using the human breast cancer cell line MBA-MB-231. As shown in Fig. 3(b), PEG–Ag_2S did not cause significant damage on the MBA-MB-231 cells after culturing for 72 h. In contrast, both the DOX@PEG–Ag_2S and free DOX can effectively induce MBA-MB-231 cell death, indicating that DOX can be effective released from PEG–Ag_2S and the encapsulation of DOX into PEG–Ag_2S does not affect its therapeutic efficacy.

Escaping from the non-specific uptake by RES and retaining a long blood circulation time are important in order to achieve the targeted delivery of a drug to the tumor tissue. It has been reported that a PEG coating can reduce rapid clearance by the liver and spleen and prolong blood circulation of nanomaterials *in vivo* [31, 35]. Therefore, the blood circulation time of DOX@PEG–Ag_2S was measured. After injection of DOX@PEG–Ag_2S into healthy nude mice through the tail vein with a DOX dosage of 15 mg/kg, 10 μL of blood samples were sequentially drawn from the mice at different time points and quantified by fluorescence intensity. Figure S4 (in the ESM) shows that DOX@PEG–Ag_2S possesses an ultralong half-life of $t_{1/2}$ = 10.3 h in the blood. The reduced RES uptake and prolonged blood circulation time of DOX@PEG–Ag_2S, originating from the surface PEG coating, should provide more opportunity for their specific accumulation in tumors.

In addition to being a successful drug carrier, the very bright fluorescence in the NIR-II window of DOX@PEG–Ag_2S enables it serve as an *in vivo* fluorescence probe to visualize the dynamical process of drug delivery to the tumor tissue and the subsequent tumor suppression. A portion of 200 μL of DOX@PEG–Ag_2S with a DOX dosage of 15 mg/kg was intravenously injected into a female athymic nude mouse with a

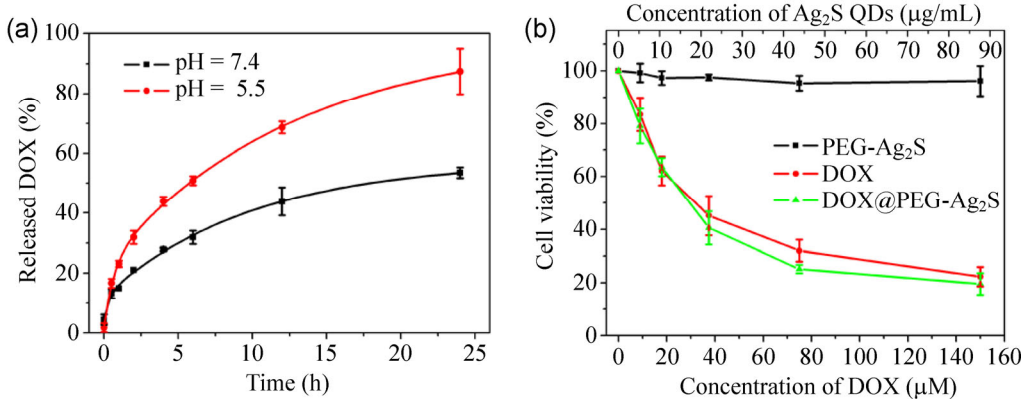

Figure 3 *In vitro* drug release and cell viability measurement. (a) DOX release curves from PEG–Ag_2S over time in PBS buffers at pH 7.4 and pH 5.5. (b) Concentration-dependent cell viability of MDA-MB-231 cells treated with free DOX, PEG–Ag_2S, and DOX@PEG–Ag_2S under *in vitro* culture conditions for 72 h.

subcutaneous xenograft MDA-MB-231 breast tumor located on the right hind limb, and an intense fluorescence signal was collected immediately under an excitation of 808 nm with an illumination density of 45 mW/cm^2 (see the real-time video in the ESM). After entering the venous blood from the tail vein, DOX@PEG–Ag_2S was carried to the heart and lung by pulmonary circulation in the first 3 s, followed by systemic circulation in other tissues and organs. Interestingly, starting at 6.8 s the tumor can be distinguished by the localized NIR-II fluorescence signal that further accumulated over time. Thus video-rate NIR-II fluorescence imaging based on Ag_2S QDs is an effective diagnosis tool to pinpoint the location of the tumor. Principal component analysis (PCA) further helped distinguish the organs and the tumor based on the dynamic contrast after computation on the first 100 frames of fluorescence images up to 15 s post injection (the arrow in Fig. S5, in the ESM).

To dynamically track the distribution of DOX@PEG–Ag_2S in living mice, we monitored the NIR-II fluorescence signal over a long period of time up to 24 h post injection (Fig. 4). Because of the EPR effect of the tumor vasculature, a steady increase of NIR-II fluorescence of Ag_2S QDs in the tumor region and a decrease of NIR-II fluorescence in other organs and skin was observed, leading to an increased tumor-to-background ratio (TBR) over time. The highest TBR of the NIR fluorescence signal was clearly observed at 9 h post-injection (Fig. 4(g)), indicating the highest tumor uptake of DOX@PEG–Ag_2S, which was determined to be approximately 8.9% ID/gram by ICP–MS. The brightfield and fluorescence images of the excised organs are shown in Fig. S6 (in the ESM), and also confirm the high accumulation of DOX@PEG–Ag_2S in the tumor site.

Confocal fluorescence images of tumor sections show the *in vivo* release of DOX from DOX@PEG–Ag_2S after it was delivered to the tumor tissue. As shown in Figs. 5(a) and 5(b), the brightfield image and the NIR-II fluorescence image of the section of tumor overlap completely, suggesting the release and even distribution of DOX in the tumor tissue. The coincidence of the Hoechst staining of the nuclei of MDA-MB-231 cells and the DOX fluorescence further confirmed the targeted delivery and release of DOX in the tumor tissue.

Thanks to the high sensitivity and high tissue

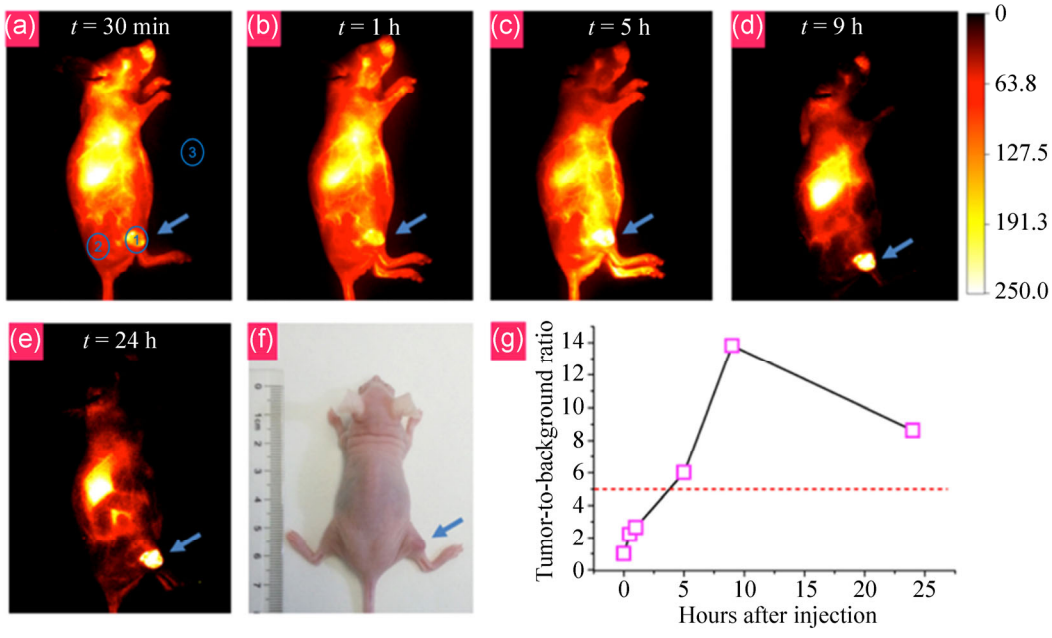

Figure 4 Time course and tumor-to-background ratio (TBR) of NIR-II fluorescence. (a)–(e) Time course of NIR-II fluorescence images of the mouse injected with DOX@PEG–Ag_2S. (f) Optical image of MDA-MB-231 tumor-bearing mouse. (g) The tumor-to-background ratio (TBR) over time determined by NIR-II fluorescence intensities utilized following formula: TBR = (Intensity of tumor – mean of noise intensity)/(Intensity of background – mean of noise intensity). The regions selected as intensity of tumor (1), background (2), and noise (3) are labeled in (a).

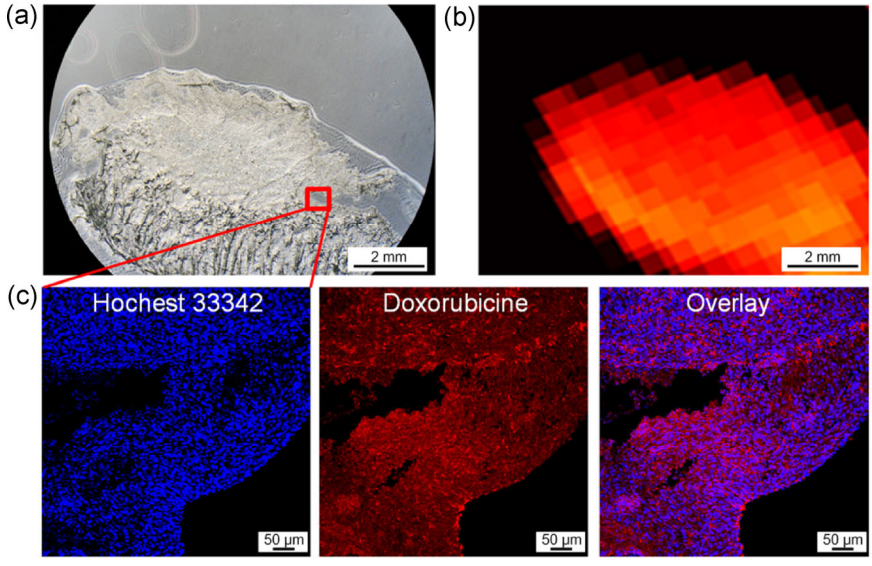

Figure 5 *In vivo* drug delivery. (a) Brightfield, (b) NIR-II and (c) confocal fluorescence images of tumor sections excised from the MDA-MB-231 tumor-bearing mouse after intravenous injection with DOX@PEG–Ag_2S for 24 h.

penetration of the NIR-II fluorescence of Ag_2S QDs, the *in vivo* real-time monitoring of tumor therapy by DOX@PEG–Ag_2S can be achieved. DOX@PEG–Ag_2S was administered to a group of mice via five tail vein injections of DOX with a dose of 15 mg/kg at day 1, 4, 7, 10 and 13, to monitor the dynamic process of tumor therapy, with another control group treated with PEG–Ag_2S. The NIR-II images of mice were collected 24 h after each injection. As shown in Fig. 6(a), PEG–Ag_2S and DOX@PEG–Ag_2S were both efficiently targeted to the tumor tissue with high TBR and the tumor tissues were clearly profiled by the bright fluorescence of Ag_2S QDs. By correlating the tumor sizes obtained from the NIR-II fluorescence images and vernier caliper measurements at different times, a high agreement was obtained (Fig. 6(b)), which indicates that the fluorescence image can precisely represent the real size of the tumor, allowing real-time *in vivo* monitoring of the tumor by NIR-II fluorescence. Note that the DOX@PEG–Ag_2S group showed a remarkable inhibition of tumor growth of approximately 70% in comparison with the control group on day 14, which further demonstrates that DOX@PEG–Ag_2S acts as an efficient drug delivery system for effective tumor therapy.

Taking advantage of the high drug loading capacity, highly targeted delivery and on-demand release in the tumor tissue of DOX@PEG–Ag_2S, the therapeutic

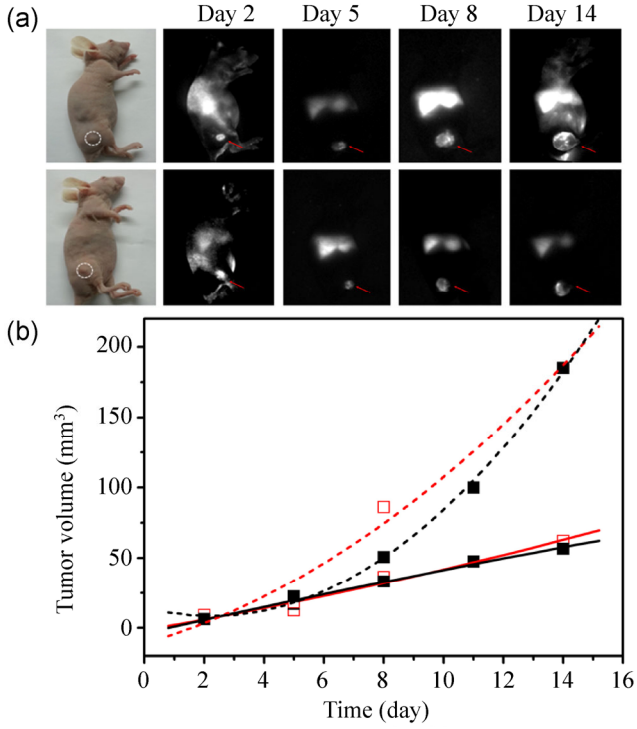

Figure 6 Real-time feedback of NIR-II fluorescence in tumor-bearing mice. (a) NIR-II images of tumor-bearing mice treated with PEG–Ag_2S (upper row) and DOX@PEG–Ag_2S (bottom row) at different times. Red arrows indicate MDA-MB-231 breast-cancer tumors. (b) Correlation of quantified tumor volume by NIR-II imaging (black) and vernier caliper measurement (red) over time from mice treated with PEG–Ag_2S (dashed line) and DOX@PEG–Ag_2S (solid line). Tumor volume was estimated according to the formula $V = 0.52ab^2$, where a is the largest superficial diameter and b is the smallest superficial diameter.

efficacy of DOX@PEG–Ag_2S on human breast tumors in living mice was systematically evaluated. Twenty-four mice bearing MDA-MB-231 breast tumors were randomly sorted into four groups and then treated five times with PBS, PEG–Ag_2S, DOX or DOX@PEG–Ag_2S at different time points (day 1, 4, 7, 10 and 13). Fig. 7(a) shows photographs of tumors collected from mice on day 21 after tumor grafting. The group treated with DOX@PEG–Ag_2S clearly showed minimum tumor growth. Weighing the tumors to precisely reflect the tumor-suppression, as shown in Fig. 7(b), showed that the group treated with DOX@PEG–Ag_2S exhibited a remarkable tumor suppression of 86%, which is much higher than the PEG–Ag_2S group and higher than the DOX group. These results clearly illustrate that DOX@PEG–Ag_2S is an efficient anticancer drug for *in vivo* tumor treatment, in addition to allowing real-time visualization of the drug delivery, targeting and therapy dynamics. Further, an *in vivo* toxicity study (Fig. 7(c)) did not show any significant tissue damage, necrosis, or inflammation of the heart, liver or kidney of mice after intravenous injection with PBS or DOX@PEG–Ag_2S for 24 h, suggesting the high biocompatibility of PEG–Ag_2S as a drug carrier.

4 Conclusions

A smart nanoplatform of DOX@PEG–Ag_2S has been successfully developed, integrating drug delivery, tumor microenvironment-response drug release and NIR-II fluorescence imaging, for real-time *in vivo* visualization of tumor theranostics. The as-prepared DOX@PEG–Ag_2S exhibited high drug loading capability (DOX, 93 wt.% with respect to Ag_2S QDs) and high

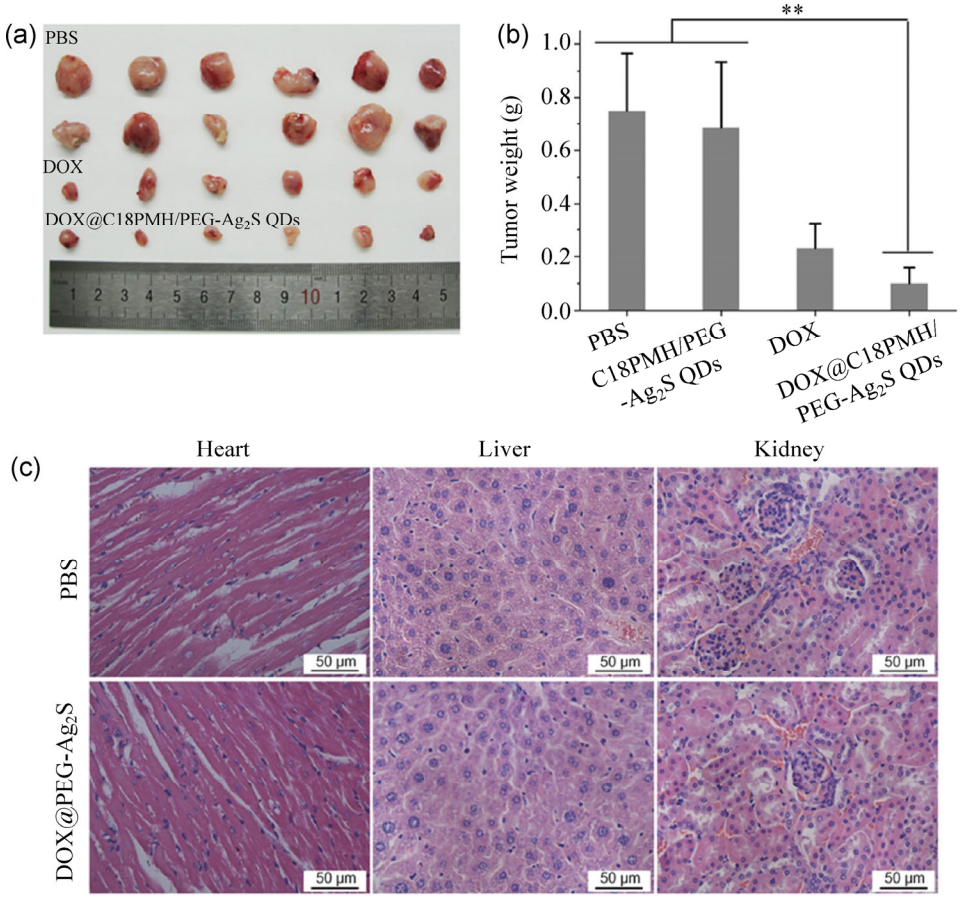

Figure 7 *In vivo* therapeutic effect and histological examination. (a) Excised tumors from mice euthanized after the 21st day of treatment by PBS, PEG–Ag_2S, DOX, and DOX@PEG–Ag_2S. (b) Tumor weight inhibition results from each treatment group corresponding to (a) $^{**}P < 0.01$. (c) Histological examination of heart, liver and kidney of mice after intravenous injection with PBS or DOX@PEG–Ag_2S for 24 h.

passive tumor-targeting efficiency (8.9% ID/gram) in living mice. In addition, DOX can be selectively and rapidly released from the Ag_2S cargoes into cancer cells due to the acidic microenvironment in a tumor, giving rise to significant tumor inhibition. Owing to the deep tissue penetration and high spatio-temporal resolution of NIR-II fluorescence imaging of Ag_2S QDs, the DOX@PEG–Ag_2S enabled real-time reading of the *in vivo* therapeutic efficacy. We expect that as a novel theranostic nanoplatform, DOX@PEG–Ag_2S—offering simultaneous diagnosis, therapy, and real-time imaging—will be highly useful for the personalized treatment of tumors.

Acknowledgements

This work was financially supported by the Chinese Academy of Sciences "Strategic Priority Research Program" (No. XDA01030200), the Ministry of Science and Technology of China (No. 2011CB965004), the National Natural Science Foundation of China (Nos. 21303249, 21301187, and 81401464), and the Natural Science Foundation of Jiangsu Province (Nos. BK2012007 and BK20130366).

Electronic Supplementary Material: Supplementary material (TEM image of DT–Ag_2S, UV–vis–NIR absorbance and fluorescence emission spectra, blood circulation of DOX@PEG–Ag_2S, time course and principal component analysis (PCA), brightfield and fluorescence images of tissues and organs of the mouse injected with DOX@PEG–Ag_2S, photo-thermal effect of Ag_2S) is available in the online version of this article at http://dx.doi.org/10.1007/s12274-014-0653-2.

References

[1] Siegel, R.; Naishadham, D.; Jemal, A. Cancer statistics, 2013. *CA: Cancer J. Clin.* **2013**, *63*, 11–30.

[2] Gregoriadis, G. Engineering liposomes for drug delivery: Progress and problems. *Trends Biotechnol.* **1995**, *13*, 527–537.

[3] O'Brien, M. E. R.; Wigler, N.; Inbar, M.; Rosso, R.; Grischke, E.; Santoro, A.; Catane, R.; Kieback, D. G.; Tomczak, P.; Ackland, S. P.; et al. Reduced cardiotoxicity and comparable efficacy in a phase III trial of pegylated liposomal doxorubicin HCl (CAELYX™/Doxil®) versus conventional doxorubicin for first-line treatment of metastatic breast cancer. *Ann. Oncol.* **2004**, *15*, 440–449.

[4] Duncan, R. The dawning era of polymer therapeutics. *Nat. Rev. Drug Discov.* **2003**, *2*, 347–360.

[5] Duncan, R. Polymer conjugates as anticancer nanomedicines. *Nat. Rev. Cancer* **2006**, *6*, 688–701.

[6] Lee, J. E.; Lee, N.; Kim, T.; Kim, J.; Hyeon, T. Multifunctional mesoporous silica nanocomposite nanoparticles for theranostic applications. *Acc. Chem. Res.* **2011**, *44*, 893–902.

[7] Shen, D. K.; Yang, J. P.; Li, X. M.; Zhou, L.; Zhang, R. Y.; Li, W.; Chen, L.; Wang, R.; Zhang, F.; Zhao, D. Y. Biphase stratification approach to three-dimensional dendritic biodegradable mesoporous silica nanospheres. *Nano Lett.* **2014**, *14*, 923–932.

[8] Terentyuk, G.; Panfilova, E.; Khanadeev, V.; Chumakov, D.; Genina, E.; Bashkatov, A.; Tuchin, V.; Bucharskaya, A.; Maslyakova, G.; Khlebtsov, N.; et al. Gold nanorods with a hematoporphyrin-loaded silica shell for dual-modality photodynamic and photothermal treatment of tumors *in vivo*. *Nano Res.* **2014**, *7*, 325–337.

[9] Yoo, D.; Lee, J.-H.; Shin, T.-H.; Cheon, J. Theranostic magnetic nanoparticles. *Acc. Chem. Res.* **2011**, *44*, 863–874.

[10] Ling, D.; Park, W.; Park, S.-J.; Lu, Y.; Kim, K. S.; Hackett, M. J.; Kim, B. H.; Yim, H.; Jeon, Y. S.; Na, K.; et al. Multifunctional tumor pH-sensitive self-assembled nanoparticles for bimodal imaging and treatment of resistant heterogeneous tumors. *J. Am. Chem. Soc.* **2014**, *136*, 5647–5655.

[11] Xing, R. J.; Bhirde, A. A.; Wang, S. J.; Sun, X. L.; Liu, G.; Hou, Y. L.; Chen, X. Y. Hollow iron oxide nanoparticles as multidrug resistant drug delivery and imaging vehicles. *Nano Res.* **2013**, *6*, 1–9.

[12] Qian, X. M.; Peng, X. H.; Ansari, D. O.; Yin-Goen, Q.; Chen, G. Z.; Shin, D. M.; Yang, L.; Young, A. N.; Wang, M. D.; Nie, S. M. *In vivo* tumor targeting and spectroscopic detection with surface-enhanced raman nanoparticle tags. *Nat. Biotechnol.* **2008**, *26*, 83–90.

[13] Rosi, N. L.; Mirkin, C. A. Nanostructures in biodiagnostics. *Chem. Rev.* **2005**, *105*, 1547–1562.

[14] Hu, M.; Chen, J. Y.; Li, Z.-Y.; Au, L.; Hartland, G. V.; Li, X. D.; Marquez, M.; Xia, Y. N. Gold nanostructures: engineering their plasmonic properties for biomedical applications. *Chem. Soc. Rev.* **2006**, *35*, 1084–1094.

[15] Dreaden, E. C.; Mackey, M. A.; Huang, X. H.; Kang, B.; El-Sayed, M. A. Beating cancer in multiple ways using nanogold. *Chem. Soc. Rev.* **2011**, *40*, 3391–3404.

[16] Zhang, B.; Price, J.; Hong, G. S.; Tabakman, S. M.; Wang, H. L.; Jarrell, J. A.; Feng, J.; Utz, P. J.; Dai, H. J. Multiplexed cytokine detection on plasmonic gold substrates with enhanced near-infrared fluorescence. *Nano Res.* **2013**, *6*, 113–120.

[17] Liu, Y.; Yin, J.-J.; Nie, Z. H. Harnessing the collective properties of nanoparticle ensembles for cancer theranostics. *Nano Res.* **2014**, *7*, 1719–1730.

[18] Cheng, L.; Wang, C.; Feng, L. Z.; Yang, K.; Liu, Z. Functional nanomaterials for phototherapies of cancer. *Chem. Rev.* **2014**, *114*, 10869–10939.

[19] Allen, T. M.; Cullis, P. R. Drug delivery systems: Entering the mainstream. *Science* **2004**, *303*, 1818–1822.

[20] Bakueva, L.; Gorelikov, I.; Musikhin, S.; Zhao, X. S.; Sargent, E. H.; Kumacheva, E. PbS quantum dots with stable efficient luminescence in the near-IR spectral range. *Adv. Mater.* **2004**, *16*, 926–929.

[21] Wehrenberg, B. L.; Wang, C. J.; Guyot-Sionnest, P. Interband and intraband optical studies of PbSe colloidal quantum dots. *J. Phys. Chem. B* **2002**, *106*, 10634–10640.

[22] Dong, B. H.; Li, C. Y.; Chen, G. C.; Zhang, Y. J.; Zhang, Y.; Deng, M. J.; Wang, Q. B. Facile synthesis of highly photoluminescent Ag_2Se quantum dots as a new fluorescent probe in the second near-infrared window for *in vivo* imaging. *Chem. Mater.* **2013**, *25*, 2503–2509.

[23] Welsher, K.; Liu, Z.; Sherlock, S. P.; Robinson, J. T.; Chen, Z.; Daranciang, D.; Dai, H. J. A route to brightly fluorescent carbon nanotubes for near-infrared imaging in mice. *Nat. Nanotechnol.* **2009**, *4*, 773–780.

[24] Hong, G. S; Diao, S.; Chang, J. L; Antaris, A. L.; Chen, C. X.; Zhang, B.; Zhao, S.; Atochin, D. N.; Huang, P. L.; Andreasson, K. I.; et al. Through-skull fluorescence imaging of the brain in a new near-infrared window. *Nat. Photonics* **2014**, *8*, 723–730.

[25] Du, Y. P.; Xu, B.; Fu, T.; Cai, M.; Li, F.; Zhang, Y.; Wang, Q. B. Near-infrared photoluminescent Ag_2S quantum dots from a single source precursor. *J. Am. Chem. Soc.* **2010**, *132*, 1470–1471.

[26] Zhang, Y.; Hong, G. S.; Zhang, Y. J.; Chen, G. C.; Li, F.; Dai, H. J.; Wang, Q. B. Ag_2S quantum dot: A bright and biocompatible fluorescent nanoprobe in the second near-infrared window. *ACS Nano* **2012**, *6*, 3695–3702.

[27] Hong, G. S.; Robinson, J. T.; Zhang, Y. J.; Diao, S.; Antaris, A. L.; Wang, Q. B.; Dai, H. J. *In vivo* fluorescence imaging with Ag_2S quantum dots in the second near-infrared region. *Angew. Chem. Int. Ed.* **2012**, *51*, 9818–9821.

[28] Chen, G. C.; Tian, F.; Zhang, Y.; Zhang, Y. J.; Li, C. Y.; Wang, Q. B. Tracking of transplanted human mesenchymal stem cells in living mice using near-infrared Ag_2S quantum dots. *Adv. Funct. Mater.* **2014**, *24*, 2481–2488.

[29] Li, C. Y.; Zhang, Y. J.; Wang, M.; Zhang, Y.; Chen, G. C.; Li, L.; Wu, D. M.; Wang, Q. B. *In vivo* real-time visualization of tissue blood flow and angiogenesis using Ag_2S quantum dots in the NIR-II window. *Biomaterials* **2014**, *35*, 393–400.

[30] Zhang, Y. J.; Liu, Y. S.; Li, C. Y.; Chen, X. Y.; Wang, Q. B. Controlled synthesis of Ag_2S quantum dots and experimental determination of the exciton Bohr radius. *J. Phys. Chem. C* **2014**, *118*, 4918–4923.

[31] Prencipe, G.; Tabakman, S. M.; Welsher, K.; Liu, Z.; Goodwin, A. P.; Zhang, L.; Henry, J.; Dai, H. J. PEG branched polymer for functionalization of nanomaterials with ultralong blood circulation. *J. Am. Chem. Soc.* **2009**, *131*, 4783–4787.

[32] Wang, C.; Cheng, L.; Liu, Z. Drug delivery with upconversion nanoparticles for multi-functional targeted cancer cell imaging and therapy. *Biomaterials* **2011**, *32*, 1110–1120.

[33] Yao, L. M.; Zhou, J.; Liu, J. L.; Feng, W.; Li, F. Y. Iridium-complex-modified upconversion nanophosphors for effective LRET detection of cyanide anions in pure water. *Adv. Funct. Mater.* **2012**, *22*, 2667–2672.

[34] Gao, Y.; Chen, Y.; Ji, X. F.; He, X. Y.; Yin, Q.; Zhang, Z. W.; Shi, J. L.; Li, Y. P. Controlled intracellular release of doxorubicin in multidrug-resistant cancer cells by tuning the shell-pore sizes of mesoporous silica nanoparticles. *ACS Nano* **2011**, *5*, 9788–9798.

[35] Ballou, B.; Lagerholm, B. C.; Ernst, L. A.; Bruchez, M. P.; Waggoner, A. S. Noninvasive Imaging of Quantum Dots in Mice. *Bioconjugate Chem.* **2004**, *15*, 79–86.